Research Square

Preprints are preliminary reports that have not undergone peer review.
They should not be considered conclusive, used to inform clinical practice,
or referenced by the media as validated information.

3D atomic structure reveals evolution of prions in templated amplification in vitro

Jan Bieschke

j.bieschke@ucl.ac.uk

University College London

Adam Wenborn

University College London https://orcid.org/0009-0009-3414-7821

Ioanna Chatzitheodosiou

University College London https://orcid.org/0009-0002-7390-4513

Kezia Jack

University College London

Mark Batchelor

University College London

Leyang Chen

University College London

Parvin Ahmed

University College London

George Thirlway

University College London

Szymon Manka

University College London

Graham Jackson

University College London

Jonathan Wadsworth

University College London https://orcid.org/0000-0002-4797-2259

John Collinge

University College London

Article

Keywords:

Posted Date: March 20th, 2026

DOI: https://doi.org/10.21203/rs.3.rs-9083455/v1

License: This work is licensed under a Creative Commons Attribution 4.0 International License.
Read Full License

Additional Declarations: Yes there is potential Competing Interest. J.C is director, J.D.F.W. and G.S.J. are shareholders of D-Gen Ltd., an academic spin-out company working in the field of prion disease diagnosis, decontamination and therapeutics. D-Gen supplied the ICSM35 and ICSM18 antibodies used for Western blot and ELISA performed in this study. The other authors declare no potential conflicts of interest.

3D atomic structure reveals evolution of prions in templated amplification *in vitro*

Adam Wenborn[1], Ioanna C. Chatzitheodosiou[1], Kezia Jack[1], Mark Batchelor[1], Leyang Chen[1], Parvin Ahmed[1], George Thirlway[1], Szymon W. Manka[1,2], Jonathan D.F. Wadsworth[1], Graham S. Jackson[1], John Collinge[1], Jan Bieschke[1]*

[1]MRC Prion Unit at UCL, UCL Institute of Prion Diseases, London, W1W 7FF, United Kingdom.

[2]Current address: Department of Infectious Disease - Faculty of Medicine, Imperial College London, London SW7 2AZ, United Kingdom.

*To whom correspondence should be addressed: j.bieschke@ucl.ac.uk

Abstract

Biological and pathological properties of prion strains are determined by fibril structure. We replicated murine RML prions through serial protein misfolding cyclic amplification (PMCA) using recombinant PrP substrate supplemented by PrP null mouse brain homogenate to probe whether fibril structure, infectivity and prion strain characteristics are conserved. Recombinant prion populations were purified and analysed for the sizes of proteinase-K resistant PrP fragments, their infectivity profile in murine cell lines, single particle spectral fingerprinting and through 3D structural reconstruction by cryo-electron microscopy.

While recombinant prions retained high specific infectivity, we found that fibril structures and biological strain properties mutated during amplification *in vitro*, leading to a novel prion strain, which is related to, but distinct from RML. Spectral and infectivity profiles suggested a convergence of prions derived from RML, ME7 and 22L prion seeds when amplified *in vitro*. These findings suggest a structural evolution of prion strains through imperfect templating, in which replication environment and substrate are major drivers of replication fitness.

Background

Prions are the proteinaceous infectious agents in prion diseases, such as Creutzfeldt-Jakob disease, scrapie and chronic wasting disease [1-3]. Prions replicate autocatalytically in a templating mechanism by incorporating cellular prion protein (PrP^C) into amyloid fibrils, which fragment to form templates for further fibril growth [4-7]. Amyloid from other protein misfolding diseases, such as Alzheimer and Parkinson's disease and systemic amyloidosis can replicate by the same prion mechanism *in vitro* [8,9], *in cellulo* [10,11], and *in vivo* [12-15]. Distinct prion strains differ in their incubation time in animals, their deposition patterns of PK-resistant aggregates in the brain and their host range in animals and cell lines [16 17].

Replication of prions via protein misfolding cyclic amplification (PMCA, [5]) using *ex vivo* prion seeds and brain homogenate from uninfected animals as substrate generates prions *in vitro,* which have the same resistance to proteinase-K (PK) digestion and the same infectivity as prion isolated *ex vivo*. Numerous systems were developed to further reduce the complexity of the system for prion replication *in vitro* [18 19 20 21 22] (reviewed in: [23]), which identified polyanionic molecules such as nucleic acids, dextran sulphate and anionic lipids as co-factors in prions replication. However, *in vitro* replication systems produced fibrils with varying specific infectivity

and PK-resistant cores [23,24], suggesting that prion replication *in vitro* may have a lower templating fidelity than replication *in vivo* and that replication of infectious prions may compete with other PrP amyloid formed either through imperfect templating, secondary nucleation [25] or *de novo* generation[22].

Prions can adapt to selection pressures in a changing environment in cell culture [26] and *in vivo*, which is most often observed when transmitting a prion across species barriers, where it has to incorporate PrP molecules with a different sequence [2 27] . In strain adaption, incubation times typically shorten through multiple passages of transmission until one or more distinct phenotypes emerge, which can be stably transmitted in further passages [28,29]. It has long been discussed whether prion strain adaption proceeds via selection from a preexisting conformer population or via 'mutation' of a single conformer through imperfect templating [2]. Occurrence of both simultaneously would result in prion structural evolution via the same Darwinian principles formulated for replication of nucleic acids *in vitro*[30]. Here, mutations generate a 'cloud' of sequences, or quasispecies, in which the replication fitness of individual species is similar under given conditions. A change in selection pressure shifts this population, leading to adaption and evolution of the quasispecies.

We tested whether an analogous process can be observed in prion replication *in vitro*. Amplification of RML scrapie prions PMCA with recombinant substrate in brain homogenate from $PrP^{-/-}$ mice resulted in PK-resistant PrP-species which could be purified to yield fibrils with specific infectivity closely similar to the RML seed. Analysis of the 3D-structure and biological activity of these fibrils revealed evolution of the prions during *in vitro* replication into a species with a distinct structure and infectivity profile. Single particle spectral analysis revealed dispersed fibril populations with different spectral characteristics suggesting the replication of a population of competing prion conformers analogous to viral quasispecies.

Results

Amplification of prions from recombinant PrP substrate

We adapted the PMCA protocol to the amplification of prions from recombinant PrP at high efficiency by substituting wild type (WT) mouse brain homogenate with that of $PrP^{-/-}$ transgenic mice and adding recombinant mouse PrP at a final concentration of 8 µM (Figure 1a, b). Serial PMCA reactions seeded with brain homogenate of RML prion-infected mice (2% w/v) yielded robust amplification of PK-resistant PrP with a ~18 kD fragment as the main PK-resistant species after 3-4 generations (Figure 1c, Supplementary Figure 1). These PMCA products could be isolated to high purity using a modified version of the prion rod purification protocol developed by Wenborn et al. [31] (Figure 1d, e), which formed fibrils visible in cryo-EM images similar to those from *ex vivo* preparations, albeit with negligible helical twist (Figure 1F).

Mass spectrometry (MS) revealed that fibrils consisted of two main PrP fragments spanning aa 89-231 and 81-231 of PrP, respectively (Supplementary Figure 2). Both MS and Western blotting with a panel of anti-PrP antibodies revealed a number of shorter PrP fragments as minor species, some of which spanned the N-terminal (aa 96-159) lobe, others the C-terminal (134-231, 153-231) lobe of the RML fibril structure (Supplementary Figures 1 and 2). sPMCA products and purified recombinant prion fibrils had specific infectivity titers identical to the RML seed ($>10^9$ LD_{50} / mg PrP) when assessed in the PK1 cell line, which is susceptible to RML prions[16] (Figure 1g).

3D-reconstruction of synthetic prion fibrils

Extensive efforts at 2D classification confirmed the initial observations from raw micrographs that the purified fibrils from the sPMCA reactions had a negligible and/or variable helical twist that could not be reliably resolved. Since established techniques for the reconstruction of amyloid fibril structures are reliant on the imposition of helical symmetry during refinement, we developed a custom analysis pipeline. Based on the assumption that the protein fold in fibrils isolated from sPMCA were similar or identical to the original *ex vivo* RML seed, we first generated an untwisted density map based on the *ex vivo* RML structure (EMD-13989,[32]) and produced lateral projections of the density map at 5° intervals of rotation (Supplementary Figure 3). Then we manually matched and aligned the 2D classes from the sPMCA dataset to these reference projections to assign relative rotational angles and lateral offset values to the particles comprising each class. These particles were back-projected in 3D space to generate an initial 3D model, which was then further refined using RELION 5.0. This approach generated a 3D map of the non-twisted fibrils at 3.45 Å resolution, sufficient to unambiguously assign an atomic model of the mouse PrP sequence (residues T94-Y225; Figure 2a-c).

Like the structure of the original RML prion strain, fibrils consisted of a parallel in-register intermolecular β-sheet amyloid core spanning residues T94 to Y225. Its rungs consisted of single PrP chains spaced at 4.71 Å with an N-terminal (aa 94-168) and a C-terminal (aa169-225) lobe in a staggered conformation (Supplementary Figure 5). The conformation of the N-terminal lobe was indistinguishable from the original RML strain (Figure 2d, e, f). The extra (non-protein) densities in the N-terminal lobe are consistent with phosphotungstate (PTA) polyanions ($[PW_{11}O_{39}]^{7-}$ at pH 7.8) used to facilitate prion purification[33]. These were previously shown not to affect conformations of prion fibrils isolated *ex vivo*[32,34]. However, the C-terminal lobe of the recombinant prion fibril deviated substantially from *ex vivo* RML, with the peptide backbone adopting cis-conformations at T187 and M204, creating a kinked structure instead of a straight hairpin (Figure 2d, e, f). In this conformation residues D201, K203, E206, R207 and E210 form an extended salt bridge, likely stabilizing the C-terminal lobe.

Structural and biological evolution of prions

The original infectivity titers calculated from the infection of PK1 cells suggested that the biological activity of recombinant prions was unchanged from RML. When we tested both prions in a panel of cell infectivity assays, however, it emerged that, while infectivity profiles were highly similar in PK1, CAD5 cell lines and a lack of infectivity to R33 cells, recombinant prions had lost the ability to infect LD9 cells (Figure 3a). This implies that amplification of RML prions *in vitro* has produced a prion with distinct structure and infectivity, i.e. a novel prion strain.

To see how this distinct prion strain emerged, we next analyzed the structural and biological evolution of fibril species during serial PMCA in a panel of assays. First, we followed the infectivity profiles in PK1 and LD9 cell lines over ten generations of serial PMCA (Figure 3b). Comparison between the abundance of prion fibrils having the full PK-resistant core (~18 kD) (Figure 2b, yellow) with infectivity profiles in PK1 and LD9 cells identified three distinct phases: 1) low infectivity, low PK-resistance (gen 1-3), 2) high PK-resistance with high infectivity in both cell lines (gen 4-6), 3) loss of LD9 infectivity while retaining PK-resistance (gen 7-10).

These data suggest the presence of different fibril populations during replication, which compete in subsequent PMCA generations. Products from serial PMCA were purified at lower PK concentration (10 µg / ml) to visualize PrP species with low PK-resistance in phase 1 of the evolution of prion populations. Under these conditions, Western blotting revealed a number of PK-resistant species with different core sizes, which emerged and disappeared during serial amplification (Supplementary Figure 1).

We then analyzed fibril structures in prion populations through the spectral shift of the amyloidophilic dye Amytracker540 when bound to different amyloid structures for single prion particles to generate a picture of the evolution of fibril populations during serial PMCA (Figure 4a, Supplementary Figure 6). While the original RML fibril had a fairly narrow, monomodal distribution in their spectral profile, distributions of subsequent generations were much broader, suggesting the presence on multiple fibril species and / or conformers. Furthermore, there was a distinct shift in the populations at gen 4-5 coinciding with the emergence of the 18kD fibrils as the dominant species. Notably, however, the mean of fibril populations continued to shift in generations 6-10, likely reflecting the emergence of fibrils which has lost their infectivity to LD9 cells as the dominant prion species, which was reflected in the similarity matrix between fibril populations (Figure 4b).

To test whether the initial prion seed or the environment and substrate determined the outcome of prion evolution *in vitro*, we compared the spectral characteristics of recombinant prions amplified through sPMCA from RML prions with sPMCA products initiated by two other prion strains, ME7 and 22L (Figure 4c, d). When analyzed by spectral fingerprinting using Amytracker 540 dye, prion fibrils isolated from RML, ME7 and 22L scrapie brain homogenate each had distinct spectral fingerprints (Figure 4c, d)[35]. In contrast, all recombinant prions converged on near-identical fingerprints, which were distinct from the original prion strains. Similarly, all three recombinant prions produced identical glycosylation patterns when further amplified in PMCA reactions using glycosylated PrP^C from Tg20 transgenic mouse brain homogenate as substrate (Figure 4e). Finally, titration of prions into the PK1 cell line, likewise, demonstrated that the biological profile of all three strains had converged (Figure 4f), strongly suggesting that replication conditions *in vitro* drove prion evolution to a single optimal species.

Discussion

3D reconstruction of fibrils at high resolution requires coverage from all angles. For well-ordered helical structures, such as twisted amyloid fibrils, this task has been automated in the RELION software [36]. Despite recent advances in helical indexing from images of fibrils much shorter than its crossover length, the reconstruction of non-helical fibrils remains challenging [25]. In our data analysis, we followed the approach of classical single particle analysis by generating 2D class averages from a large number of randomly oriented particles [37]. Multiple approaches have been developed to solve the difficult problem of assigning 2D classes to specific orientations [38]. Here, we were greatly aided by the assumption of a 3D structure similar to the known structure of *ex vivo* RML fibrils [32,34], which allowed us to manually assign orientations based on their similarity to projections of an untwisted fibril model. It is conceivable that future analysis can predict the relative orientation of two projection images[39], removing the need for a known structural scaffold, which would greatly expand the scope of this approach.

All 3D structures of scrapie-derived prion fibrils share a common two-lobe PIRIBS architecture with similar folds of the N-terminal lobe [32,34,40,41], while the angle between N- and C-terminal lobe and the interactions of the C-terminal tail of PrP varied significantly [42], suggesting a higher degree of conformational flexibility. C-terminal lobes consist of a single hairpin or kinked structure linked by the disulfide bond between C178 and C213. Depending on the strain, the C-terminal tail forms a stable interaction with either the N-terminal or the C-terminal lobe. Compared to the C-terminal lobe, the N-terminal lobe presents a more densely packed multistrand structure [42]. It is plausible that the common architecture of the N-terminal lobe reflects the fact that all of these strains evolved from sheep scrapie prions through multiple passaging in different rodent species [43]. Notably, CWD prion fibrils, while retaining the two-lobe structure, displayed an entirely different N-terminal fold [44]. All structures of PrP amyloid fibrils generated *in vitro* from recombinant protein, which have been solved so far, did not share this common architecture, but rather consisted of amyloid cores that folded into single hairpin structures or extended anti-parallel dimers and included only short N- or C-terminal sequences of the prion protein[45-50].

Both our study and the accompanying manuscript from the Soto laboratory found that replication of RML prions in PMCA reactions, albeit under different reaction conditions, generated infectious prion fibrils, which shared the two-lobe structure of *ex vivo* prions, suggesting that this structural arrangement is a prerequisite for PrP prion infectivity *in vivo*. Both studies find that the C-terminal lobe folds into a kinked conformation, that is distinct from all other rodent strains analyzed so far (Figure 3).

It has long been discussed, whether cellular co-factors are required for the generation and replication of prions [1]. *De novo* fibril formation [22] and prion replication studies in minimal buffer systems [18-21] have reported the generation of infectious PrP fibrils with the help of anionic lipids, nucleic acids or other poly-anionic molecules (reviewed in : [23]). These molecules, similar to the co-factors provided in the $PrP^{-/-}$ brain homogenate used in our study, may provide a scaffold orienting positively charged lysine residues in the prion fibril [51]. In contrast, fibrils of α-synuclein generated *de novo,* which caused pathology of multiple system atrophy in transgenic and WT mice, did not require the presence of co-factors to guide fibril assembly *in vitro* [52].

The variability of specific infectious titers of PrP fibrils generated *de novo* [23], suggests that these systems are more permissive to the replication of a population of amyloid structures with different folds and different specific infectivity. Two hypotheses, which are not mutually exclusive, may account for this observation: One, the amplification environment may be less stringent for lack of protein quality control and degradation pathways present in cells [53]. This would select for the amplification of faster growing fibril species over those, which are more resistant to degradation. Two, the lack of glycosylation of PrP substrate alters the fitness landscape in prion replication, either in terms of fibril growth or stability. Thus, glycosylation may suppress the formation of PrP fibril species with smaller amyloid cores, which have not been reported from PMCA reactions using glycosylated *ex vivo* PrP^{C} as substrate. At the same time, templating with *ex vivo* prions favors the formation of infectious prions with an extended amyloid core, as seen in our study, even in the absence of PrP glycosylation.

We observed that both structural and biological properties of the fibril population changed in the course of multiple generations of prion replication in serial PMCA with recombinant PrP substrate. While PK-resistant species with smaller amyloid cores appeared early in replication, fibrils with aa94-225 amyloid core dominated during later sPMCA generations. Notably, the infectivity profile further evolved in generations 4-10, while PK-resistant species generated from recombinant PrP were already abundant and amplifying robustly. Similar structural evolution has

been observed during the *de novo* fibril formation of tau protein and IAPP, which saw changing populations of competing amyloid species[25,54].

Our data provide new evidence in the longstanding discussion whether prion strain adaption proceeds via selection from a preexisting conformer population, via 'mutation' of a single conformer through imperfect templating or via Darwinian evolution which combines both processes [2,30,35]. The N-terminal lobe of the recombinant prion fibrils is identical to the structure seed RML strain, which is similar but not identical to that of ME7 and 22L prions [42]. This strongly suggests that the synthetic structure is derived from the primary RML structure via imperfect templating leading to 'structural mutation' of the fibril. This interpretation is supported by the change in biological activity profile late in the serial PMCA reaction. While rare, we observed such structural mutations during the elongation of single synthetic PrP fibrils *in vitro*[35]. At the same time, selection between replicating amyloid species is the inevitable result of different reaction kinetics and limited substrate availability in PMCA, as in any other autocatalytic process *in vitro* or *in vivo* [35].

Alternatively, a sub-strain could be present in RML as a minor component of the fibril population. However, a minor prion species would either die out during many generations of passaging *in vivo* or become dominant, unless its replication fitness is finely balanced with that of the major prion strain conformer, or unless it is constantly regenerated through structural mutations by imperfect templating during replication.

Furthermore, we observed that spectral and biological properties of the RML, ME7 and 22L strains derived from sheep scrapie [28,43] converged in serial PMCA reactions. This observation implies that the synthetic prions formed from these strains possess structures, which present the same binding interfaces to the Amytracker dye and to the cellular binding partners responsible for the different susceptibilities of cell lines to different prion strains. This does not necessarily mean that the whole of the prion structure is identical, though, as it is currently unknown which structural elements are responsible for binding of LCO dyes and cell infectivity, respectively. The most parsimonious explanation of our data suggests that prion strains consist of an ensemble of related conformers with similar replication fitness in a given environment. While reported cryo-EM structural data suggests few major conformers [55], the abundance and diversity of minor conformers cannot currently be assessed. The ensemble is maintained by imperfect templating during replication, analogous to the quasispecies theory of nucleic acid replication [30].

Methods

Research governance

Work at UCL was conducted in the Unit's microbiological containment level 3 (CL3) or level 2 (CL2) facilities with strict adherence to risk assessments and safety protocols. Cryo-EM analysis at Birkbeck College London was performed in CL2 laboratories using dedicated sample holders and equipment with strict adherence to safety procedures and local risk assessment as described previously [60]. Work with mice was performed under approval and licence granted by the UK Home Office (Animals (Scientific Procedures) Act 1986) (Project LicencePP3260075) and conformed to UCL institutional and ARRIVE guidelines (www.nc3rs.org.uk/ARRIVE/). All protocols and procedures at UCL involving animals were approved by the MRC Prion Unit at University College London Animal Welfare and Ethical Review Body.

Prion sources

Brains from RML- and ME7-infected CD1 and C57BL/6JOlaHsd mice were sourced from previously reported transmission studies [31,41,32]. The 22L prion strain was supplied to the Unit from the TSE Resource Centre, Roslin Institute, University of Edinburgh and amplified by intracerebral inoculation of C57BL/6JOlaHsd mice, as described previously for RML and ME7 prion strains[31]. Brains from terminally affected mice were used to prepare 10% (w/v) RML, ME7 and 22L brain homogenates in Dulbecco's phosphate buffered saline lacking Ca^{2+} or Mg^{2+} ions (D-PBS; Thermo Fisher Cat. No. 14190-086).

sPMCA

3-month-old PrP-KO mice line F10 with the FVB genotype (Harlan) [56] were ethically culled and perfused with ice cold 1 x Dubelco's PBS without Ca^{2+}, without Mg^{2+} + 5mM EDTA before excision of brains. Brain homogenates were prepared as 18% w/v in ice cold 2x Conversion Buffer (122 mM Tris-HCl pH 7.4, 12 mM EDTA, 732 mM NaCl, 2.44% v/v Triton X-100, 2 x Protease Complete (Roche, Cat No 1836145)) with a Dounce, glass homogeniser. The homogenate was mixed with an equal volume of 0.5 mg/ml recombinant mPrP23-231 in PBS, centrifuged at 1000g for 60 s. The supernatant is removed taking care to avoid the soft pellet, aliquoted and frozen at -70°C.

80µl reaction mix was pipetted into a PCR tube (Star Lab, cat no I1402-2800) or plate containing 3 x 0.5mm diameter zirconium beads (BioSpec, cat no 11079105z). Initial reactions were seeded by 1.6 µl RML, ME7 or 22L brain homogenate. Samples are sonicated for 0-96 cycles consisting of 30s sonication at 50% power and 30 min rest in a QSonica Q700MPX water bath sonicator at 35°C. PMCA products were diluted 1:10 into fresh reaction mix for each generation of serial PMCA.

For PMCA using ex vivo PrP^C, 3 month old Tg20 mice [57] were perfused as described above. Homogenates were prepared as 9% w/v in ice cold Conversion Buffer (1.1 x D-PBS (Invitrogen Cat No 14200-067), 165mM NaCl, 1.1% Triton X-100, 1 x Protease Complete with EDTA (Roche Cat No 1836145)) with a Dounce glass homogeniser.

PrP expression and purification

Mouse PrP was expressed and purified as previously described [58]. Briefly, the open-reading frame of mouse PrP gene (Prnp) (residues 23-231, including S231), was synthesized de novo by Eurofins MWG Operon, with a thrombin-cleavable His-Tag added to the PrP N-terminus. The ligated pTrcHisB/PRNP and pTrcHisB/Prnp constructs were used to transform the Escherichia coli host strain BL21(DE3) (Novagen), genotype F' ompT hsdSB (rB- mB-) gal dcm (DE3), which was then plated onto Luria-Bertoni (LB) agar plates containing 100 µg/ml carbenicillin. Cultures were grown for purification using a modification of protocols previously described[59]. Cells were sonicated and their inclusion bodies resolubilized in 6 M guanidine hydrochloride (GuHCl), 50 mM Tris-HCl, 0.8% β-mercaptoethanol, pH 8.0. These were loaded onto a Ni-NTA column equilibrated in 6 M GuHCl, 10 mM Tris-HCl, 100 mM Na_2PO_4, 10 mM glutathione pH 8.0, and eluted from the column using 10 mM Tris-HCl, 100 mM Na_2PO_4, 2 M imidazole pH 5.8. Residual GuHCl was removed through dialysis against 20 mM BisTris-HCl pH 6.5, $CaCl_2$ added to a final concentration of 2.5 mM, and the N-terminal His-tag cleaved by thrombin for 16 hr at room temperature (RT) (0.1 U thrombin [Novogene]/1 mg of PrP added). The cleaved protein was loaded onto a second Ni-NTA column equilibrated with 20 mM Bis-Tris pH 6.5, 25 mM imidazole pH 6.5, and the eluted PrP peak was collected and dialyzed against 10 mM Bis-Tris pH 6.5, and aliquoted and stored at –80°C. Protein concentrations were determined by UV absorption at 280 nm using a calculated molar extinction of 62,268 M^{-1} cm^{-1} (https://web.expasy.org/protparam).

Proteinase-K digestion and Western blotting

18µl of PMCA product was thawed, thoroughly vortexed and then centrifuged at 100 x g for 1 min. 2 µl of 1 mg /ml proteinase K (Merck: Product No 390973P) was added to give a final concentration of 100µg/ml and samples incubated at 37 ˚C for 1 h shaking at 750 rpm, followed by centrifugation at 13,200 rpm (16,100 x g) for 1 min in a microfuge (Eppendorf). The digestion was terminated by resuspension of the sample with 40 µl of 2 x working SDS sample buffer (125mM Tris-HCl, 20 % v/v glycerol pH 6.8 containing 4 % w/v SDS, 4 % v/v 2-mercaptoethanol, 8mM 4-(2-aminoethyl)-benzene sulfonyl fluoride and 0.02 % w/v bromphenol blue) and immediate transfer to a 100 ˚C heating block for 10 min. All samples were centrifuged at 13,200 rpm (16,100 x g) for 1 min in a microfuge (Eppendorf), thoroughly vortexed and then re-centrifuged (13,200 rpm for 10 min) prior to electrophoresis on 12% BisTris gels (Novex: Cat No NP0342BOX) using MES (Figure 1c, d, e) or MOPS (Figure 1a, Supplementary Figure1). Pre-stained markers used are Seeblue Plus2 (Novex; LC5925). Gels were electro-blotted (one blot per Novex blot module) on to PVDF membrane (Immobilon P; Sigma Cat No P2938) at constant voltage of 35V for 2 h or 15 V overnight using an electro-blotting buffer of 20 mM Tris / 150 mM glycine containing 20 % (v/v) methanol. Immobilon P membrane was soaked for 2 min in 100 % methanol and then rinsed in electro-blotting buffer immediately prior to use.

Blot membranes were treated with 5 % (w/v) milk powder in PBST (PBS containing 0.05 % Tween20) for 1 h and then incubated with a 0.2 µg/ml of anti-PrP monoclonal antibody ICSM 35 (D-Gen Ltd), ICSM 18 (D-Gen Ltd) or 8H4 (Merck Life Science, Cat no P0110-200UL) in PBST containing 0.1 %(w/v) sodium azide for either 90 min or overnight. Following washing for 60 min with PBST, blots were incubated for 1 h with a 1:10,000 dilution of goat anti-mouse IgG-phosphatase conjugate (Biosource International; AMI3705 or Sigma A-2179) in PBST, washed for 60 min with PBST and 2 x 5 min with 20 mM Tris pH 9.8 containing 1mM $MgCl_2$ (1 x assay buffer; Tropix Inc) and developed in chemiluminescent substrate (CDP-Star; Tropix Inc) and imaged on Biomax MR Film (Kodak).

Prion rod purification

The purification protocol was modified from Wenborn et al [31]. The PMCA reaction product was digested with 10 µg/mL Proteinase K (Merck, 70663) shaking at 800 rpm for 30 min at 37°C at an Eppendorf Thermomixer comfort. The digestion was stopped by the addition of 2 mM AEBSF. Next, samples were adjusted to final concentrations of 2% (w/v) sarkosyl (Calbiochem), 0.01 U/mL of Benzonase (Merck, 70664-3) and 0.3% (w/v) sodium phosphotungstate (NaPTA, Sigma, P6395), followed by 30 min incubation at 800 rpm. Next, iodixanol (Sigma, D1556) was added to a final concentration of 45% (w/v) and the concentration of NaPTA adjusted to 0.3% (w/v) final concentration. The sample was centrifuged at 4,000 x g for 30 min, at 37 °C and 1 mL of supernatant was collected. Samples were diluted with an equal volume of PBS containing 2% sarcosyl and 0.3% NaPTA. The samples were centrifuged at 16,100 g for 90 min at 27 °C, the supernatant was removed and the pellet was resuspended in 1 mL sodium phosphate buffer (5 mM, pH 7.4) with 0.1% sarkosyl and 0.3% NaPTA and centrifuged at 16100 g for 30 minutes. The pellet was resuspended in 40 uL of PBS Purity of prion rod preparations was assessed by silver staining SDS-PAGE in NuPage Bis-Tris 12% gel, using the protocol according to the silver staining kit (SilverQuest Silver Staining Kit-1, LC6070, Life Technologies Ltd) and by Western blotting.

Preparation of cryo-EM grids

Prion fibrils from P3 pellet samples resuspended in wash buffer (see above) were directly applied to glow-discharged C-flat™ Holey Carbon CF-2/2-4C Cu 400 mesh cryo-EM grids (Electron Microscopy Sciences) in the chamber of the Leica GP2 plunging robot. Typically, 4 µl of P3 pellet suspension was applied per grid. The chamber was set to 20°C and 40% humidity. After 10 s incubation, the grids were blotted for 3 s (with an additional 2 mm push) and plunge-frozen in liquid ethane maintained at -183°C. Initial screening of cryo-EM grids was done within the Unit using a 120 kV Talos microscope (Thermo Fisher) with a tungsten filament and a 4k x 4k BM-Ceta camera.

Cryo-EM data collection

Cryo-micrographs were acquired at Birkbeck College London, on a 300 kV Krios G3i microscope (Thermo Fisher) with a post-GIF (20 eV slit) K3 detector (Gatan) operated in super-resolution bin 2x mode at 105,000 nominal magnification. The final (post-binning) magnified pixel size was 0.828 Å. The dose rate was ~20 $e^-/Å^2/s$ during 2.5-s exposures, resulting in a total dose of ~50 $e^-/Å^2$ on the specimen. The exposures were collected automatically at 5 shots per grid hole, with fast acquisition (up to ~600 images/h), using the EPU 2 software (Thermo Fisher), at defocus ranging from -2.1 to -0.6 µm, and fractionated into 50 movie frames.

Cryo-EM image processing and 3D reconstruction

A non-twisted version of the ex vivo RML density map (EMDB-13989) was generated using a python script that applies an inverse rotation to each Z-layer according to its axial position and the cumulative helical twist at that position, as determined from the refined crossover distance and voxel size. This reference was then lowpass filtered to 10 Angstrom in the z-axis using relion_image_handler to smooth out inter-rung density features. Alternatively, a similar result can be achieved using relion_helix_inimodel2d with the --only_make_3d flag, --iniref specifying an appropriate cross-section image and --crossover_distance set to a very large value. Lateral projections of this untwisted map were generated using relion_project with –tilt 90 and values for --rot at 5 degree increments between 0 and 355 degrees.

2D classification was performed in Relion 5.0 as described previously[60]. Briefly, successive rounds of 2D classification were performed at box sizes of 1280, 640 and 480 pixels and classes from the final round were filtered for those with a value for rlnEstimatedResolution less than 7.0 Å. These class views were then manually matched and aligned with the gallery of lateral projections of the non-twisted map. The highest-quality class for each lateral projection view was taken forward, and the nominal rotation angle of that view was assigned to all the particles of the matched class. An initial 3D reference was then generated from these particles using relion_reconstruct. Further 3D refinement was conducted using Relion 3D auto refinement with appropriate values for --sigma_tilt, --sigma_rot and --sigma_psi.

Structural Visualisation

Cross-sections of raw cryo-EM density maps are presented as the average of the central six layers of voxels of the refined map, corresponding to 4.968 Å or approximately one full rung of the amyloid structure. Visualisations of rendered density maps and atomic models were performed in ChimeraX[61]. Schematic representations of the atomic models were generated using atom2svg.py[62].

Cell-based prion bioassay

Prion infectivity measurement in the Cell Panel Assay was performed using four cell lines as originally described[17]. The cell lines used were; PK1/2 cells[16] (an established cell line; D-Gen Ltd London, originally derived from N2a cells that were obtained from, and authenticated by, the American Type Culture Collection (ATCC)) [16], LD9 cells[17] (an established cell line; that was a gift from Professor Charles Weissmann, originally derived from murine L929 fibroblasts supplied and authenticated by the ATCC), R33 cells[16] (an established cell line; that was a gift from Professor Charles Weissmann, originally derived from N2a cells obtained and authenticated by the ATCC), and CAD5 cells[17] (an established cell line; that was a gift from Professor Charles Weissmann, originally derived from Cath.a-differentiated (CAD) cells[63]). Study samples were serially diluted in culture medium and directly applied to cells. Cells were incubated for 3 days before being split 1:6 (v/v) into fresh cell culture media and grown back to confluence. Up to four further splits (as above) were conducted before transferring a sample of the cells to ELISPOT plates for determination of proteinase K-resistant PrP positive cells (spot counts) as described previously[16,17,24,31,64]

Single molecule spectral analysis

8-well chamber slides (Cellvis, C8-1.5H-N) were washed in Hellmanex II detergent (1:50 in water), followed by three washes with ultrapure water, a wash in 100% methanol and three more water washes. The chambers were then glow discharged for 40 s using an PELCO easiGLOW glow discharge unit (Ted Pella Inc, USA). 10 uL of each sample was added to the center of each well and dried for 1 h, washed 3 times with ultrapure water (500 µL) and 200 µL of 1:10,000 Amytracker 540 (Ebba biotech) were pipetted on top of the sample and the chamber sealed with twinsil silicone (picodent).

Images were acquired on a Total Internal Reflection Fluorescence microscope (Cairn Research; [65]) at high angle excitation at 473 nm. Fluorescence emission was split into two images in an optosplit 2 beamsplitter using the following emission filter set (525/50; dichroic 565lpxr; 595/50). The images were analyzed using a python script available at www.github.com/ioannachatzitheodosiou/Optosplit_Analysis . Briefly, the images were cropped according to the two regions of interest, then aligned using the Stackreg bilinear transformation. Afterwards, signal values from each pixel in the first image was divided by aligned pixel value of the second image. The resulting image was processed with watershed segmentation form the opencv package, which separated the aggregates from the image background. The mean intensity of the pixels and area corresponding to each particle was calculated and parsed in csv files. Fluorescence ratios and particle sizes were plotted and p values were calculated using one – way ANOVA. N = 55 to 140 particles from 15 images were analyzed for each data set. The Kruskal – Wallis test was chosen due to being non – parametrically distributed as determined by the Shapiro - Wilk test. Heatmaps of the post hoc pairwise comparison of fluorescence ratios were calculated using the Dunn – Bonferroni test.

Spectral fingerprinting

Prion rod samples were generated as outlined above and mixed with Amytracker 540 to a final dye concentration of 1 µM. Samples were mixed thoroughly and dispensed into flat bottom 96 well black plates (Corning 3474) in triplicate, with a minimum volume of 50 µL. The plate was left to incubate for ~30 minutes and then placed into a Tecan M1000 fluorescence plate reader. 3D fluorescence maps (where both excitation and emission are varied) were recorded for relevant intervals. The data was exported into an excel spreadsheet and analysed as described in [65] in R studio using a script adapted from[66].

Mass spectrometry

Intact mass spectrometry was performed by denaturing purified sPMCA fibril samples in 8.0 M urea, followed by dilution to 1.0 M urea and direct analysis by liquid chromatography–mass spectrometry using an Acquity I-Class UPLC system coupled to a Xevo G2-XS Q-ToF mass spectrometer (Waters). Data were collected in MS acquisition mode and data analysed using MaxEnt1 (Waters).

Data availability statement

The sPMCA cryo-EM density map was deposited into the Electron Microscopy Data Bank (EMDB) (https://www.ebi.ac.uk/pdbe/emdb) under accession number EMD-57062. The corresponding atomic coordinates were deposited in the Protein Data Bank (PDB) (https://www.rcsb.org) under PDB ID 29BR. The RML 3D cryo-EM density map was accessed from the EMDB under accession number EMD-13989 (Infectious mouse-adapted RML scrapie prion fibril purified from terminally infected mouse brains). The corresponding atomic coordinates were accessed from the PDB under PDB ID 7QIG. UniProt UP000000589, Mus musculus, was used as the reference proteome for mass spectrometry. Uncropped and unprocessed SDS-PAGE and Western blot data, imaging data and mass spectrometry data generated in this study are provided in the Source Data files.

Source data are provided in the Mendeley data base
https://data.mendeley.com/preview/xkzxpnwmj5?a=4920a978-9ea8-44bb-b094-a719d7fc7a1b

Acknowledgements

This work was funded by the core award to the MRC Prion Unit at UCL from the UK Medical Research Council (MC_UU_00037/7 and MC_UU_00024/6 to J.B.; MC_UU_00037/8 and MC_UU_00024/7 to J.C.; MC_UU_00024/5 and MC_UU_00037/6 to J.D.F.W; MRC Prion Unit Graduate Programme to K.J.). Cryo-EM data for this investigation were collected at the Institute of Structural and Molecular Biology Electron Microscopy facility (Birkbeck College, University of London) with financial support from the Wellcome Trust (202679/Z/16/Z, 206166/Z/17/Z and 106249/Z/14/Z)). We are very grateful to N. Lukoyanova and S. Chen at Birkbeck College for EM support, to Susan Joiner for help in brain homogenate preparation, to Elizabeth B. Sawyer for her contribution to developing the recombinant PMCA methodology, to D. Johnson and P. King at UCL for infrastructure support and the staff of the MRC Prion Unit at UCL Biological Services Facility. S.W.M is supported by an MRC Career Development Award (CDA) fellowship. JC is an NIHR Senior Investigator.

Contributions

J.B. and J.D.F.W. and J.C acquired funding and oversaw the study. J.B. administered the project. J.B. and J.D.F.W. supervised the research. G.S.J., A.W., I.C.C., J.B. and J.D.F.W. designed experiments. G.S.J., A.W., M.B., L.C. and I.C.C. performed prion replication experiments. P.A., G.T. and A.W. performed the cell-based prion bioassays. J.D.F.W. generated prion stock homogenates. A.W. developed sample purification methods. G.S.J, I.C.C. and A.W. prepared purified samples. A.W. performed the mass spectrometry. I.C.C. performed spectral analysis.

S.W.M. generated cryo-EM grids and coordinated data collection. A.W. performed cryo-EM data analysis, reconstruction of the cryo-EM map and fitting of the atomic model. S.W.M., A.W., J.B., J.D.F.W., I.C.C., J.C. and G.S.J. interpreted results. J.B. wrote the manuscript, with contributions from A.W., J.D.F.W., M.B. and I.C.C and J.C.

Ethics declarations

Competing interests

J.C is director, J.D.F.W. and G.S.J. are shareholders of D-Gen Ltd., an academic spin-out company working in the field of prion disease diagnosis, decontamination and therapeutics. D-Gen supplied the ICSM35 and ICSM18 antibodies used for Western blot and ELISA performed in this study. The other authors declare no potential conflicts of interest.

References

1. Prusiner, S.B. Prions. *Proc Natl Aca Sci USA* **95**, 13363-13383 (1998).
2. Collinge, J. & Clarke, A. A general model of prion strains and their pathogenicity. *Science* **318**, 930-936 (2007).
3. Collinge, J. Mammalian prions and their wider relevance in neurodegenerative diseases. *Nature* **539**, 217-226 (2016).
4. Lansbury, P.T. Mechanism of scrapie replication. *Science* **265**, 1510-1510 (1994).
5. Saborio, G.P., Permanne, B. & Soto, C. Sensitive detection of pathological prion protein by cyclic amplification of protein misfolding. *Nature* **411**, 810-813 (2001).
6. Bieschke, J. et al. Autocatalytic self-propagation of misfolded prion protein. *Proc. Natl. Acad Sci U. S. A* (2004).
7. Castilla, J., Saa, P., Hetz, C. & Soto, C. In vitro generation of infectious scrapie prions. *Cell* **121**, 195-206 (2005).
8. Iadanza, M.G., Jackson, M.P., Hewitt, E.W., Ranson, N.A. & Radford, S.E. A new era for understanding amyloid structures and disease. *Nat Rev Mol Cell Biol* (2018).
9. Kedia, N. et al. Desmin forms toxic, seeding-competent amyloid aggregates that persist in muscle fibers. *Proc Natl Acad Sci U S A* **116**, 16835-16840 (2019).
10. Sanders, D.W., Kaufman, S.K., Holmes, B.B. & Diamond, M.I. Prions and Protein Assemblies that Convey Biological Information in Health and Disease. *Neuron* **89**, 433-448 (2016).
11. Woerman, A.L. et al. Propagation of prions causing synucleinopathies in cultured cells. *Proc Natl Acad Sci U S A* (2015).
12. Luk, K.C. et al. Intracerebral inoculation of pathological alpha-synuclein initiates a rapidly progressive neurodegenerative alpha-synucleinopathy in mice. *J Exp Med* (2012).
13. Meyer-Luehmann, M. et al. Exogenous induction of cerebral beta-amyloidogenesis is governed by agent and host. *Science* **313**, 1781-1784 (2006).
14. Purro, S.A. et al. Transmission of amyloid-beta protein pathology from cadaveric pituitary growth hormone. *Nature* **564**, 415-419 (2018).
15. Banerjee, G. et al. Iatrogenic Alzheimer's disease in recipients of cadaveric pituitary-derived growth hormone. *Nat Med* (2024).
16. Klohn, P., Stoltze, L., Flechsig, E., Enari, M. & Weissmann, C. A quantitative, highly sensitive cell-based infectivity assay for mouse scrapie prions. *Proc Natl Acad Sci USA* **100**, 11666-11671 (2003).

17. Mahal, S.P. et al. Prion strain discrimination in cell culture: The cell panel assay. *Proc Natl Acad Sci USA* **104**, 20908-20913 (2007).
18. Deleault, N.R., Lucassen, R.W. & Supattapone, S. RNA molecules stimulate prion protein conversion. *Nature* **425**, 717-720 (2003).
19. Wang, F., Wang, X., Yuan, C.G. & Ma, J. Generating a prion with bacterially expressed recombinant prion protein. *Science* **327**, 1132-1135 (2010).
20. Legname, G. et al. Synthetic mammalian prions. *Science* **305**, 673-676 (2004).
21. Makarava, N. et al. Recombinant prion protein induces a new transmissible prion disease in wild-type animals. *Acta Neuropathol* **119**, 177 (2010).
22. Eraña, H. et al. A Protein Misfolding Shaking Amplification-based method for the spontaneous generation of hundreds of bona fide prions. *Nat Commun* **15**, 2112 (2024).
23. Jack, K., Jackson, G.S. & Bieschke, J. Essential Components of Synthetic Infectious Prion Formation De Novo. *Biomolecules* **12**(2022).
24. Schmidt, C. et al. A systematic investigation of production of synthetic prions from recombinant prion protein. *Open Biol* **5**(2015).
25. Lovestam, S. et al. Disease-specific tau filaments assemble via polymorphic intermediates. *Nature* **625**, 119-125 (2024).
26. Li, J., Browning, S., Mahal, S.P., Oelschlegel, A.M. & Weissmann, C. Darwinian evolution of prions in cell culture. *Science* **327**, 869-872 (2010).
27. Vanik, D.L., Surewicz, K.A. & Surewicz, W.K. Molecular basis of barriers for interspecies transmissibility of mammalian prions. *Mol Cell* **14**, 139-45 (2004).
28. Block, A.J. & Bartz, J.C. Prion strains: shining new light on old concepts. *Cell Tissue Res* **392**, 113-133 (2023).
29. Zemlyankina, I. et al. Genetic Variation and Strain Dynamics in Chronic Wasting Disease. *Viruses* **17**(2025).
30. Eigen, M. Selforganization of matter and the evolution of biological macromolecules. *Naturwissenschaften* **58**, 465-523 (1971).
31. Wenborn, A. et al. A novel and rapid method for obtaining high titre intact prion strains from mammalian brain. *Sci Rep* **5**, 10062 (2015).
32. Manka, S.W. et al. 2.7 Å cryo-EM structure of ex vivo RML prion fibrils. *Nat Commun* **13**, 4004 (2022).
33. Levine, D.J. et al. Mechanism of Scrapie Prion Precipitation with Phosphotungstate Anions. *ACS Chem Biol* (2015).
34. Hoyt, F. et al. Cryo-EM structure of anchorless RML prion reveals variations in shared motifs between distinct strains. *Nat Commun* **13**, 4005 (2022).
35. Sun, Y. et al. Direct Observation of Competing Prion Protein Fibril Populations with Distinct Structures and Kinetics. *ACS Nano* (2023).
36. He, S. & Scheres, S.H.W. Helical reconstruction in RELION. *J Struct Biol* **198**, 163-176 (2017).
37. Nakane, T., Kimanius, D., Lindahl, E. & Scheres, S.H. Characterisation of molecular motions in cryo-EM single-particle data by multi-body refinement in RELION. *Elife* **7**(2018).
38. Lyumkis, D. Challenges and opportunities in cryo-EM single-particle analysis. *Journal of Biological Chemistry* **294**, 5181-5197 (2019).
39. Lu, Y., Liu, J., Zhu, L., Zhang, B. & He, J. 3D reconstruction from cryo-EM projection images using two spherical embeddings. *Commun Biol* **5**, 304 (2022).
40. Kraus, A. et al. High-resolution structure and strain comparison of infectious mammalian prions. *Mol Cell* (2021).
41. Manka, S.W. et al. A structural basis for prion strain diversity. *Nat Chem Biol* (2023).
42. Manka, S.W., Wenborn, A., Collinge, J. & Wadsworth, J.D.F. Prion strains viewed through the lens of cryo-EM. *Cell Tissue Res* **392**, 167-178 (2023).

43. Kimberlin, R.H. *Slow virus diseases of animals and man*, xvi, 404 p. (North-Holland Pub. Co. ; American Elsevier, Amsterdam New York, 1976).
44. Alam, P. et al. Cryo-EM structure of a natural prion: chronic wasting disease fibrils from deer. *Acta Neuropathol* **148**, 56 (2024).
45. Glynn, C. et al. Cryo-EM structure of a human prion fibril with a hydrophobic, protease-resistant core. *Nat Struct Mol Biol* **27**, 417-423 (2020).
46. Lee, C.H. et al. The Positively Charged Cluster in the N-terminal Disordered Region may Affect Prion Protein Misfolding: Cryo-EM Structure of Hamster PrP(23-144) Fibrils. *J Mol Biol* **436**, 168576 (2024).
47. Wang, L.Q. et al. Cryo-EM structure of an amyloid fibril formed by full-length human prion protein. *Nat Struct Mol Biol* **27**, 598-602 (2020).
48. Wang, L.Q. et al. Genetic prion disease-related mutation E196K displays a novel amyloid fibril structure revealed by cryo-EM. *Sci Adv* **7**, eabg9676 (2021).
49. Chen, E.H. et al. 2.2 A Cryo-EM Tetra-Protofilament Structure of the Hamster Prion 108-144 Fibril Reveals an Ordered Water Channel in the Center. *J Am Chem Soc* **144**, 13888-13894 (2022).
50. Li, Q., Jaroniec, C.P. & Surewicz, W.K. Cryo-EM structure of disease-related prion fibrils provides insights into seeding barriers. *Nat Struct Mol Biol* **29**, 962-965 (2022).
51. Silva, J.L. et al. Experimental approaches to the interaction of the prion protein with nucleic acids and glycosaminoglycans: Modulators of the pathogenic conversion. *Methods* **53**, 306-317 (2011).
52. Burger, D. et al. Synthetic alpha-synuclein fibrils replicate in mice causing MSA-like pathology. *Nature* (2025).
53. Chen, B., Retzlaff, M., Roos, T. & Frydman, J. Cellular strategies of protein quality control. *Cold Spring Harb Perspect Biol* **3**, a004374 (2011).
54. Wilkinson, M. et al. Structural evolution of fibril polymorphs during amyloid assembly. *Cell* **186**, 5798-5811 e26 (2023).
55. Sawaya, M.R., Hughes, M.P., Rodriguez, J.A., Riek, R. & Eisenberg, D.S. The expanding amyloid family: Structure, stability, function, and pathogenesis. *Cell* **184**, 4857-4873 (2021).
56. Mallucci, G.R. et al. Post-natal knockout of prion protein alters hippocampal CA1 properties, but does not result in neurodegeneration. *EMBO J* **21**, 202-10 (2002).
57. Fischer, M. et al. Prion protein (PrP) with amino-proximal deletions restoring susceptibility of PrP knockout mice to scrapie. *EMBO J* **15**, 1255-64 (1996).
58. Sangar, D. et al. Syntaxin-6 delays prion protein fibril formation and prolongs presence of toxic aggregation intermediates. *Elife* **13**(2024).
59. Hosszu, L.L. et al. Definable equilibrium states in the folding of human prion protein. *Biochemistry* **44**, 16649-57 (2005).
60. Manka, S.W. et al. 2.7 A cryo-EM structure of ex vivo RML prion fibrils. *Nat Commun* **13**, 4004 (2022).
61. Pettersen, E.F. et al. UCSF ChimeraX: Structure visualization for researchers, educators, and developers. *Protein Sci* **30**, 70-82 (2021).
62. Nakane, T. atom2svg. (2020).
63. Qi, Y., Wang, J.K., McMillian, M. & Chikaraishi, D.M. Characterization of a CNS cell line, CAD, in which morphological differentiation is initiated by serum deprivation. *J Neurosci* **17**, 1217-1225 (1997).
64. Chan, A.S., Mowla, S.N., Arora, P. & Jat, P.S. Tumour suppressors and cellular senescence. *IUBMB Life* (2014).
65. Sun, Y. et al. Direct Observation of Competing Prion Protein Fibril Populations with Distinct Structures and Kinetics. *ACS Nano* **17**, 6575-6588 (2023).

66. Lapworth, D.J. & Kinniburgh, D.G. An R script for visualising and analysing fluorescence excitation-emission matrices (EEMs). *Computers & Geosciences* **35**, 2160-2163 (2009).

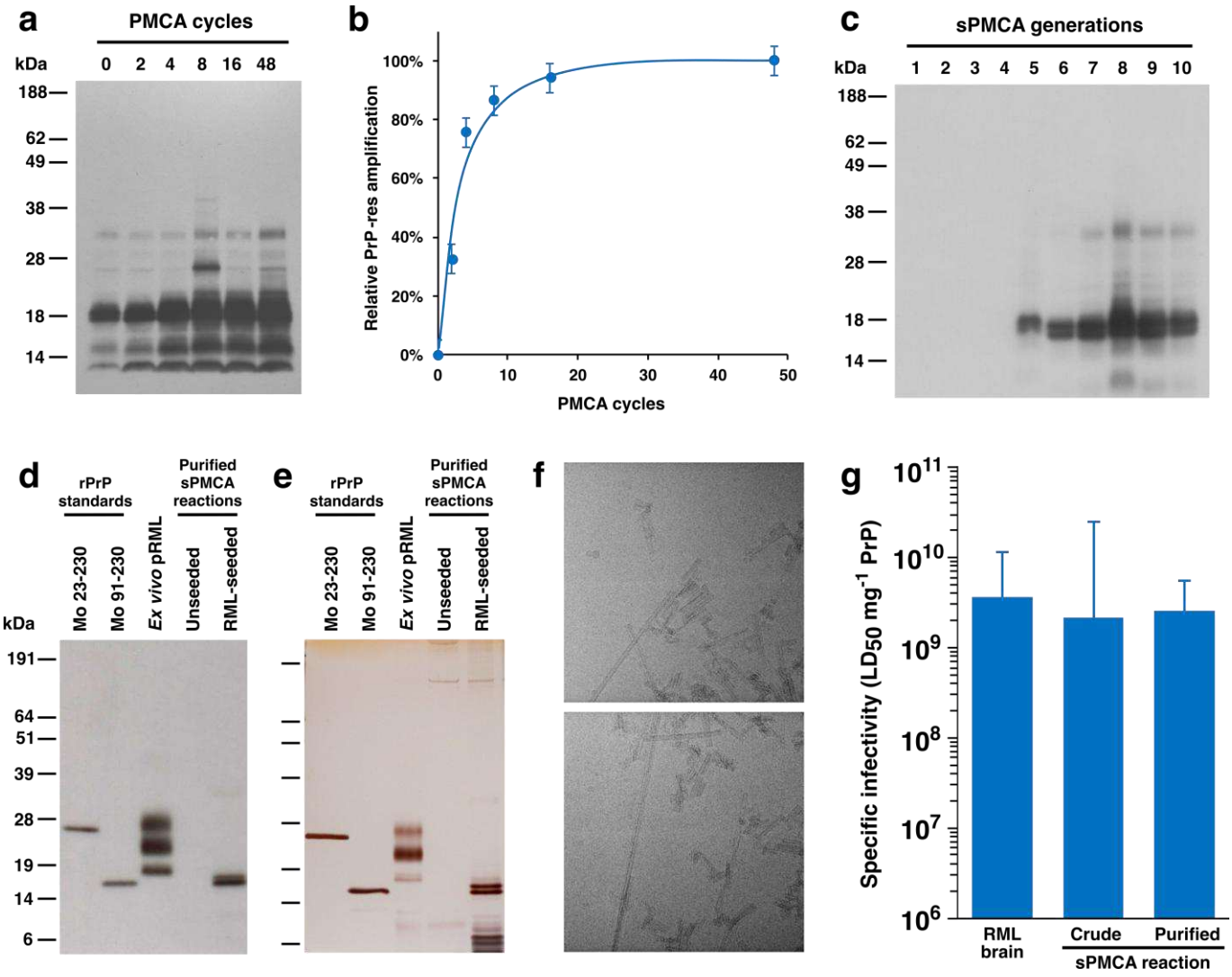


Figure 1: PMCA amplification of RML scrapie prions using recombinant mouse PrP 23-231 substrate in PrP $^{-/-}$ brain homogenate. (a) Proteinase-K (100 µg/ml, 1 h) resistant PrP species analyzed by Western blotting (ICSM35) after 0 - 48 PMCA cycles. (b) Densitometric quantification of main PMCA product (apparent MW ~16-19 kD, depending on the SDS-PAGE running buffer); error bars represent the average SD of all normalized data points from two independent experiments (n=8). (c) Western blot of PK-resistant PrP species amplified in serial PMCA reactions +/- RML seed (2%, I6200 brain homogenate). Each generation was diluted 10-fold into fresh brain homogenate / PrP mix. (d) Western blot (ICSM35) and (e) silver stain SDS-PAGE of prion rods purified from 7th generation PMCA product, (f) Cryo-EM image of sPMCA generated prion rods. (g) Specific infectivity of RML prions, sPMCA product and purified prion rods assessed using RML-susceptible mouse cell line PK1; error bars represent SD, n = 3 independent reactions.

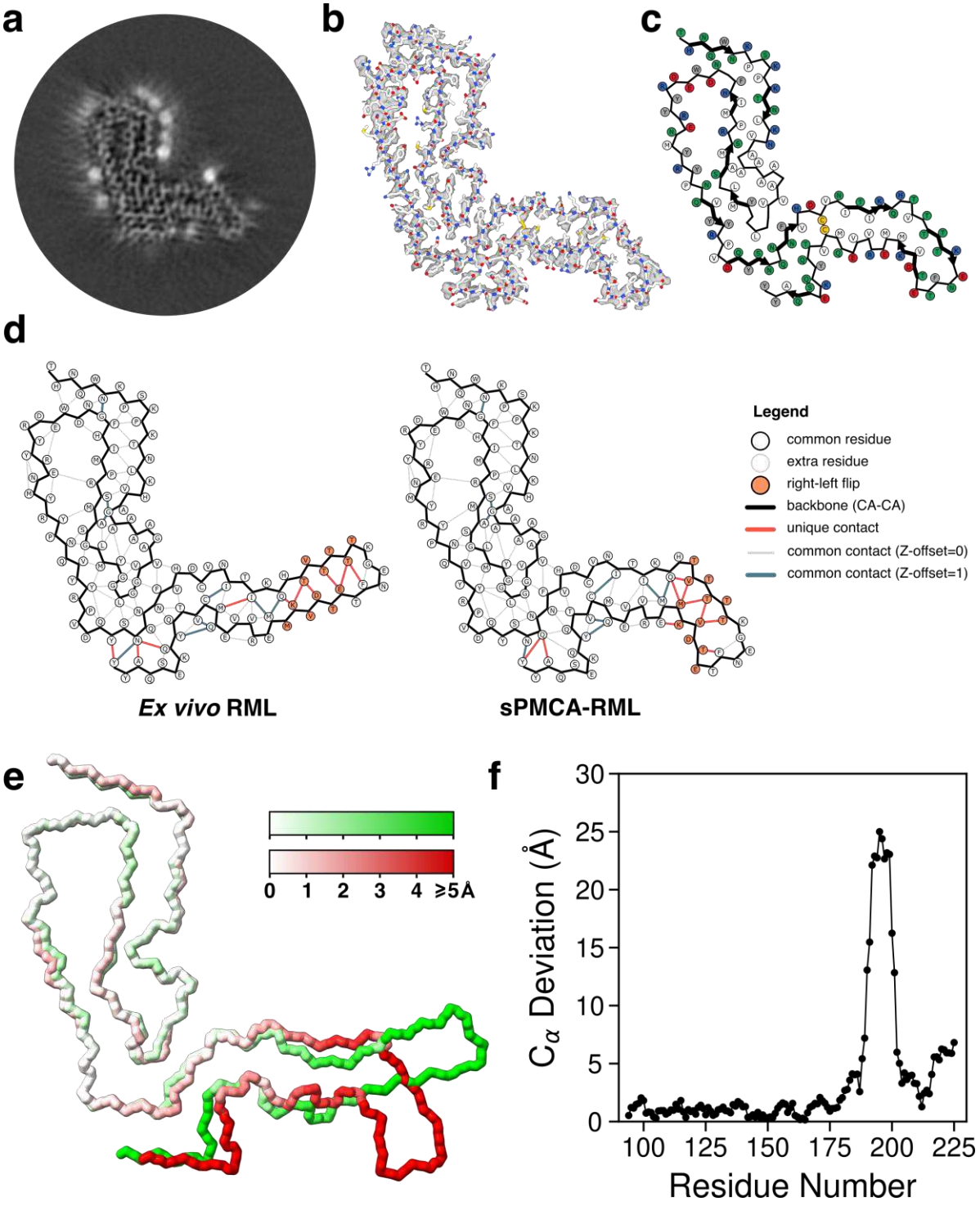


Figure 2: 3D-reconstruction of prion rods from sPMCA amplification. (a) Cross-sectional view of sPMCA fibril density map in 3D reconstruction. Bright electron densities are due to PTA^- complexed with the fibril. (b) Electron density and (c) cartoon model of sPMCA prion structure. (d) Analysis of Amyloid Packing Difference showing comparisons of sidechain interactions between *ex vivo* RML and sPMCA fibril structures. (e) Aligned peptide backbones of structures of sPMCA derived prion fibrils (red) compared to ex vivo RML (green[32]) shaded according to inter-atomic distances; (f) Plot of deviation in C_α atom positions between sPMCA and *ex vivo* RML (7QIG) fibril structures.

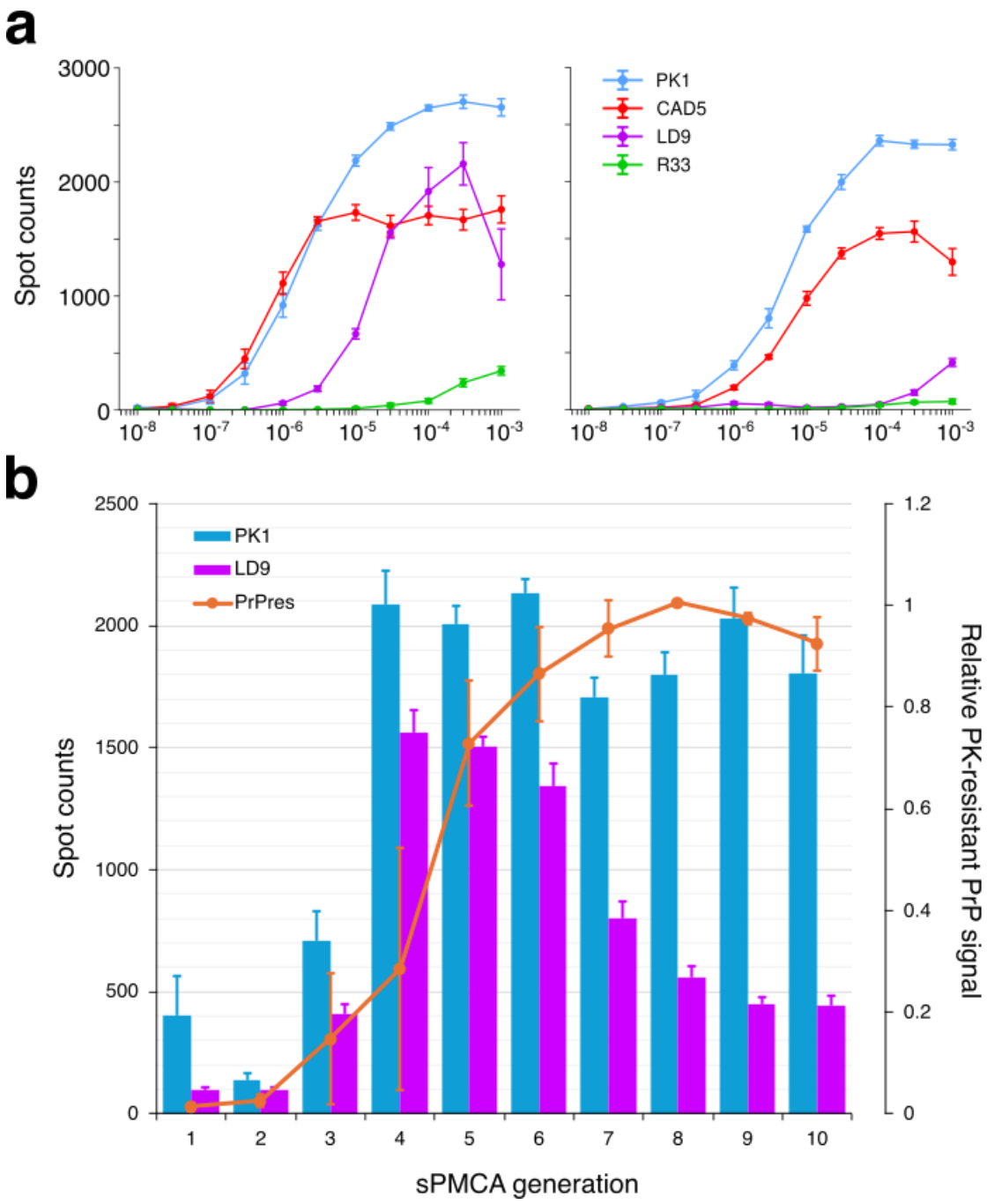


Figure 3: Distinct infectivity profiles of recombinant and RML prions. (a) Purified recombinant prion rods (sPMCA generation 7) and original RML brain homogenate were assessed in panel of cell lines with different susceptibilities to prion strains in a serial dilution experiment. Both strains infected PK1 and CAD5 cell lines, but recombinant prions lost the ability to infect LD9 cells. (b) Comparison of the abundance of full-length PK-resistant PrP amyloid (aa 94-225) over serial PMCA cycles (orange, averages of normalized densitometric data from three independent experiments) with infectivity in PK1 (blue) and LD9 (purple) cells, as reported by spot counts in the Scrapie Cell Assay (mean ± SEM, n=8). Comparison of the profiles of infectivity in these cell lines across multiple sPMCA generations shows three distinct phases, likely corresponding to different fibril populations.

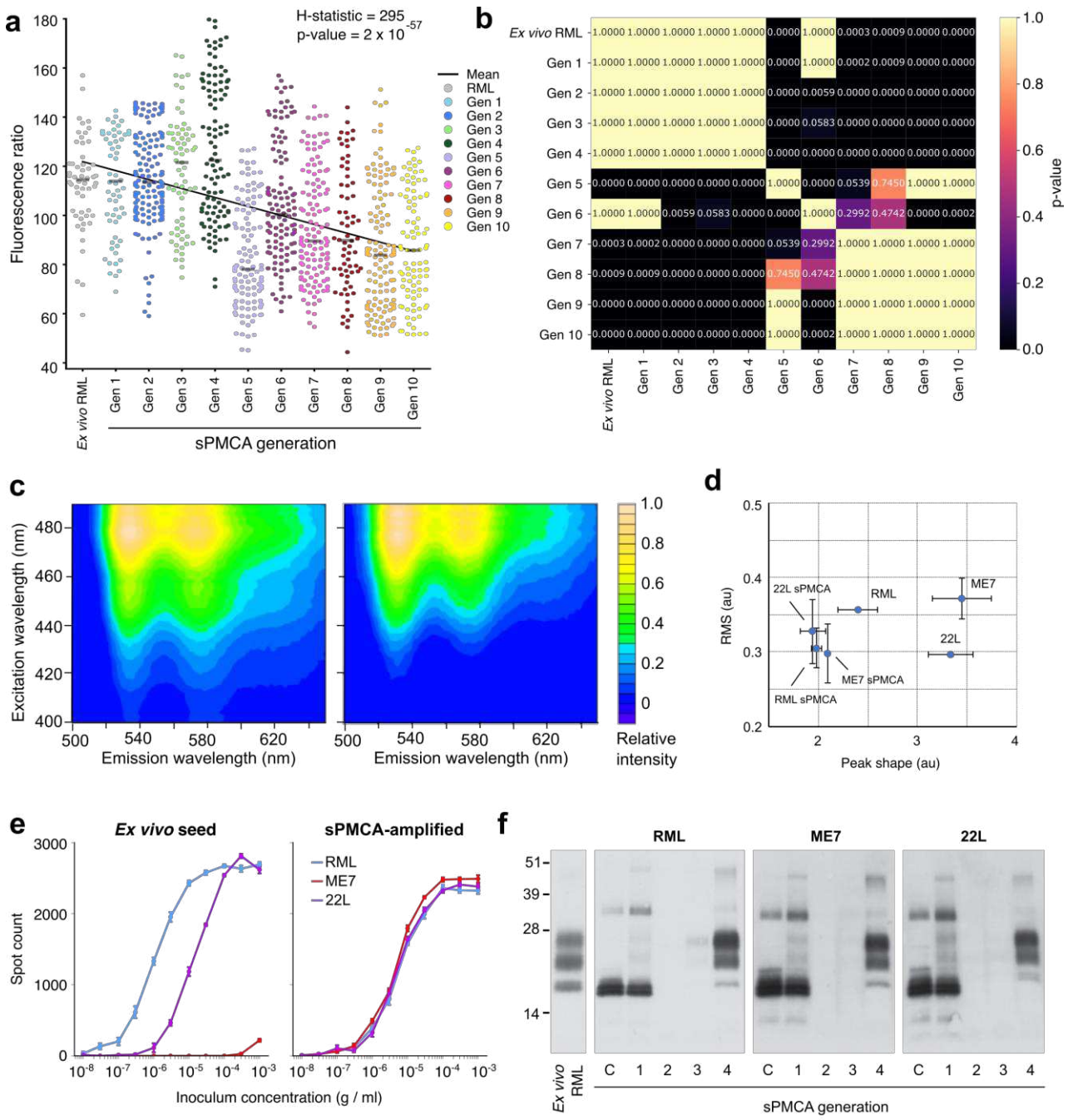
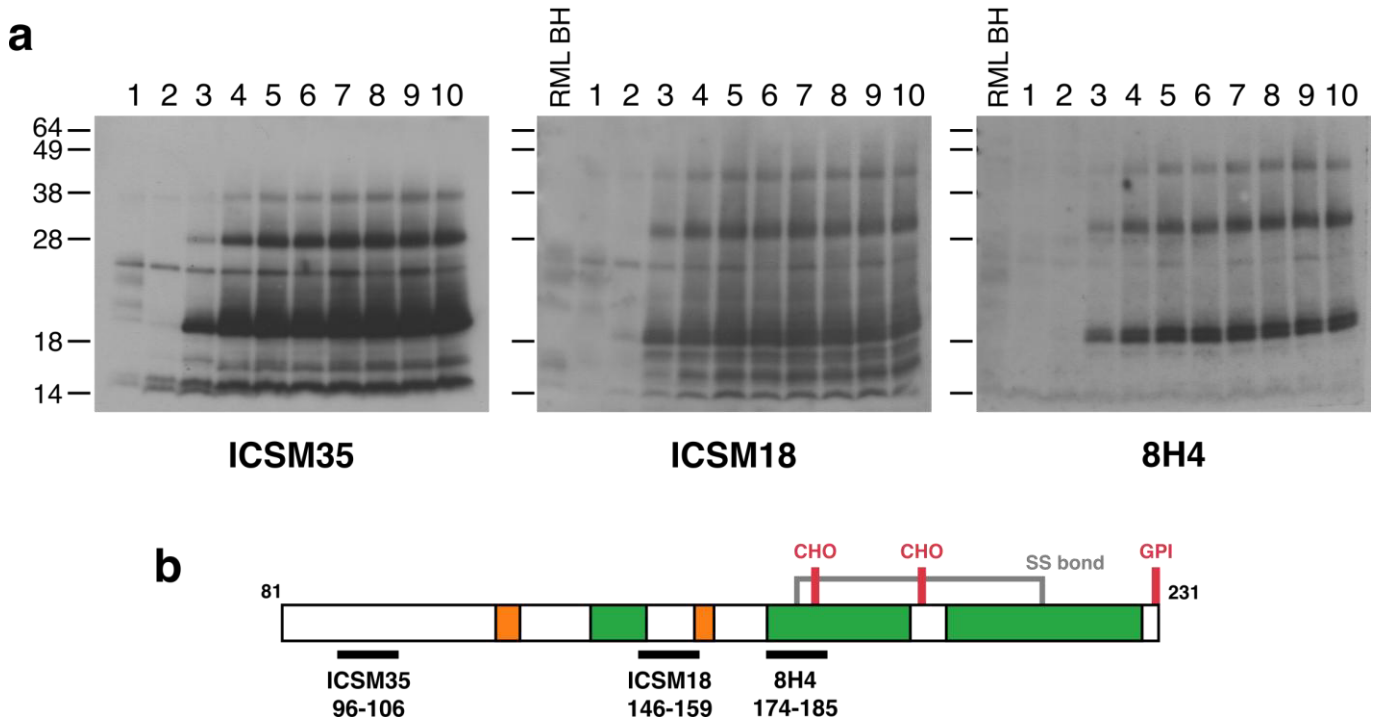


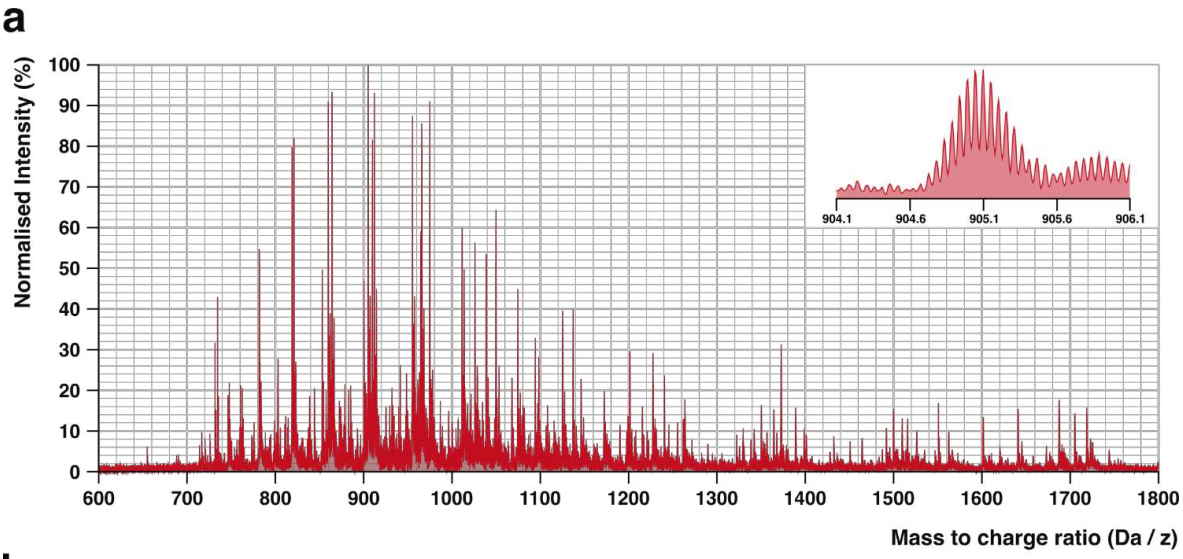
Figure 4: Structural evolution of prions analyzed by spectral fingerprinting. (a) Single particle spectral analysis of prion fibrils isolated from serial PMCA by prion rod preparation with limited PK digestion (10 µg/ml, 30 min). Fibrils were imaged by TIRF microscopy (excitation 473 nm) and Amytracker540 fluorescence was split into emission signals < 565 nm and > 565 nm. The scatter plot shows the signal ratio for each prion particle; horizontal bars represent the mean of each distribution, n = 55 - 140 particles per generation. (b) Heatmap of the post hoc comparison of fluorescence ratios using the Dunn – Bonferroni test on the data set from (A). (c) Multi-spectral fingerprinting of fibrils purified from RML brain homogenate and sPMCA gen 7. (d) Spectral fingerprinting of recombinant prion rods generated by sPMCA from RML, ME7 and 22L prions compared with prion rods isolated from original seeds; data represent mean ± SD of measurements from three independent fibril preparations. (e) Serial PMCA reaction products (generation 7) and original RML, ME7 and 22L brain homogenates were assessed in the PK1 cell lines. Infectivity profiles converged after sPMCA. (f) RML, ME7 and 22L prions were replicated by sPMCA using recombinant PrP23-231 substrate for five generations and then further replicated for four sPMCA generations using Tg20 brain homogenate as substrate. Western blotting (ICSM35) after PK digestion (100 µg/ml, 1 h) yielded identical glycosylation patterns, which were distinct from brain homogenate of RML-infected mice (I6200).

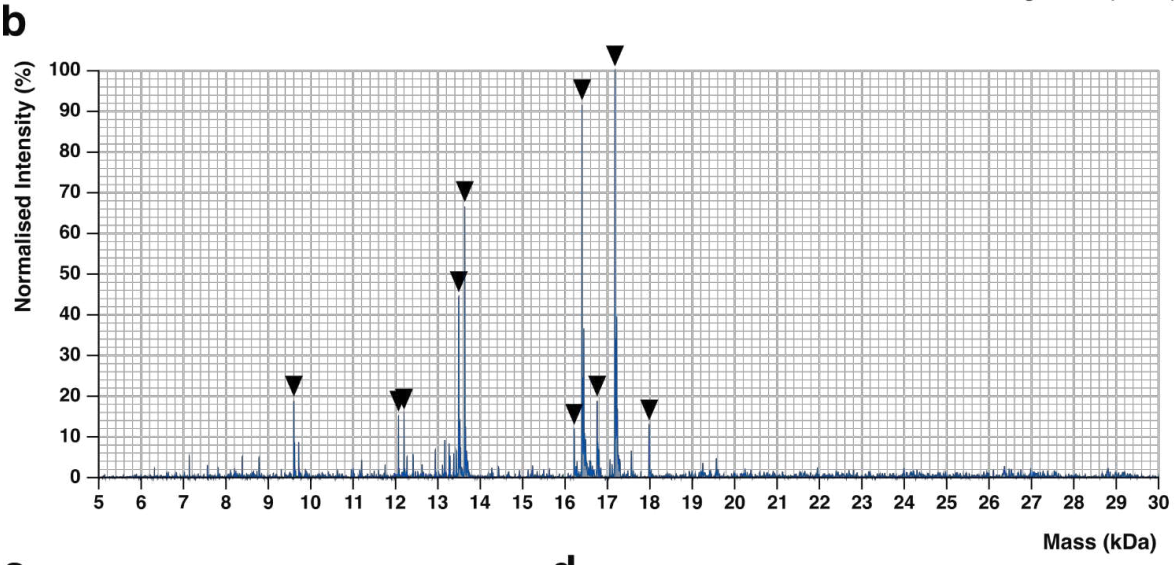
	sPMCA-RML
PDB entry	**29BR**
EMDB entry	EMD-57062
Data collection and processing	
Magnification	105,000x
Voltage (kV)	300
Electron exposure (e–/Å2)	49.4
Defocus range (μm)	-2.0 to -0.6
Pixel size (Å)	0.828
Symmetry imposed	C1
Initial particle images (no.)	1,201,178
Particle images for 3D (no.)	980,263
Final particle images (no.)	269,101
Map resolution (Å, FSC = 0.143)	3.08
Helical parameters	
Rise (Å)	-
Twist (°)	-
Crossover distance (Å)	-
Refinement	
Initial model used (PDB code)	7QIG
Model resolution (Å)	3.08
FSC threshold	0.143
Map sharpening B factor ($Å^2$)	-14.57
Model composition	
Non-hydrogen atoms	1072
Protein residues	132
B factors ($Å^2$)	
Protein	78.22 - 173.47
r.m.s. deviations	
Bond lengths (Å)	0.005
Bond angles (°)	1.123
Validation	
MolProbity score	1.92
Clashscore	6.40
Poor rotamers (%)	0.0
Ramachandran plot	
Favoured (%)	89.5
Allowed (%)	10.5
Disallowed (%)	0.0

Supplementary Table 1: Cryo-EM data collection, refinement and validation statistics.



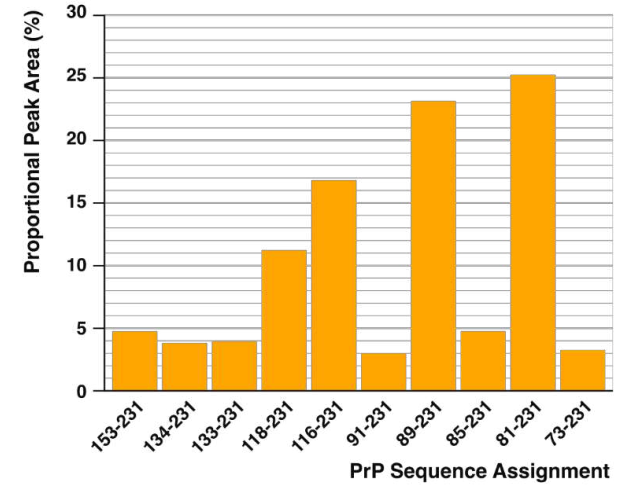
Supplementary Figure 1: PK-resistant fragments in sPMCA amplification. (a) PK (10 µg/ml) digested sPMCA products (round 1-10) probed by antibodies against different PrP regions reveal 18 kD fragments as the main species, while PK-resistant PrP fibrils with shorter amyloid cores appear as minor species at different stages of replication. (b) Schematic of the mouse prion protein sequence labelled with the epitopes of ICSM35, ICSM18 and 8H4 antibodies as used in (a); structural features of PrP^{C} are also shown, with alpha-helical regions (green), beta sheets (orange), disulfide bond (grey) and post-translational modifications (red).



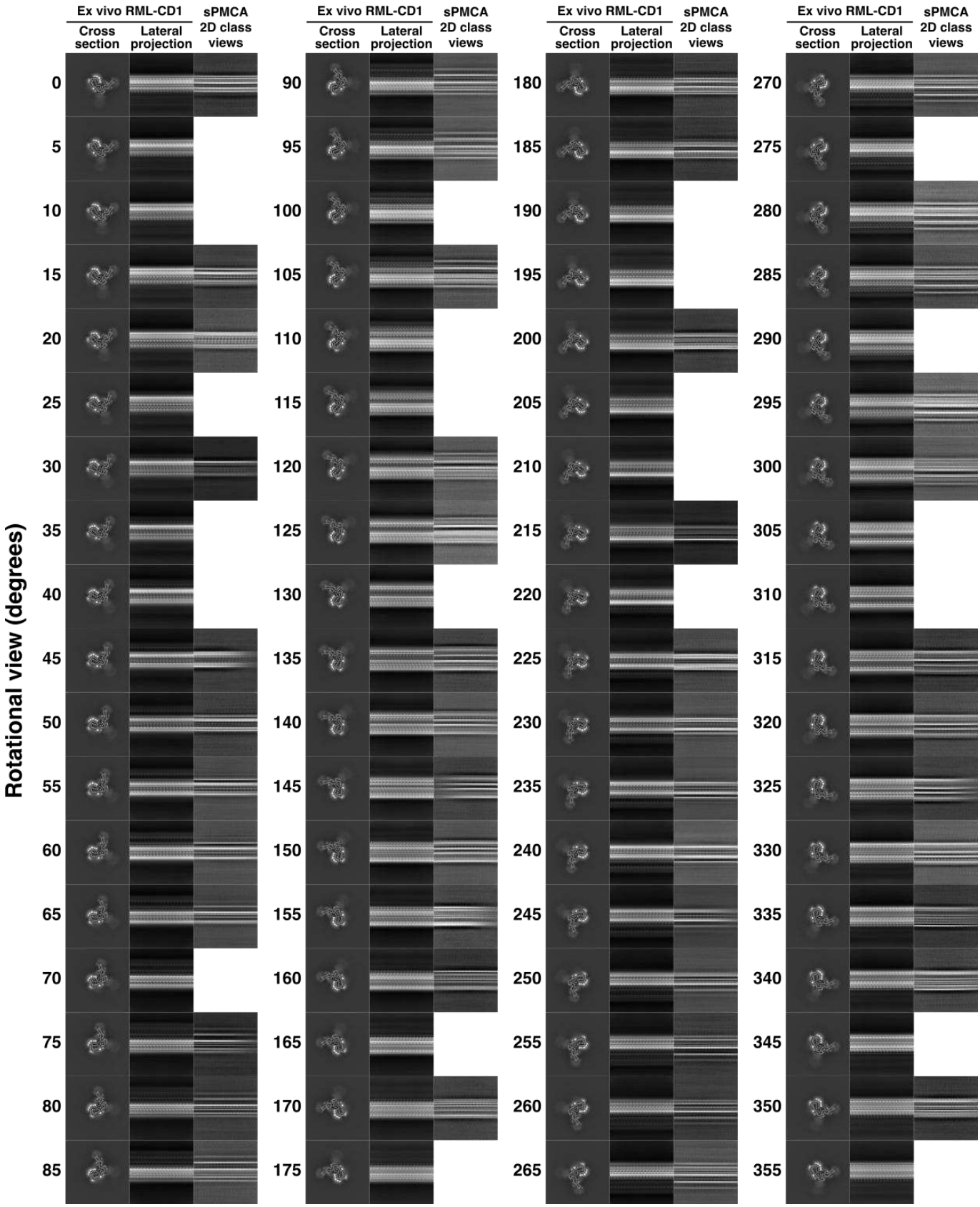


c

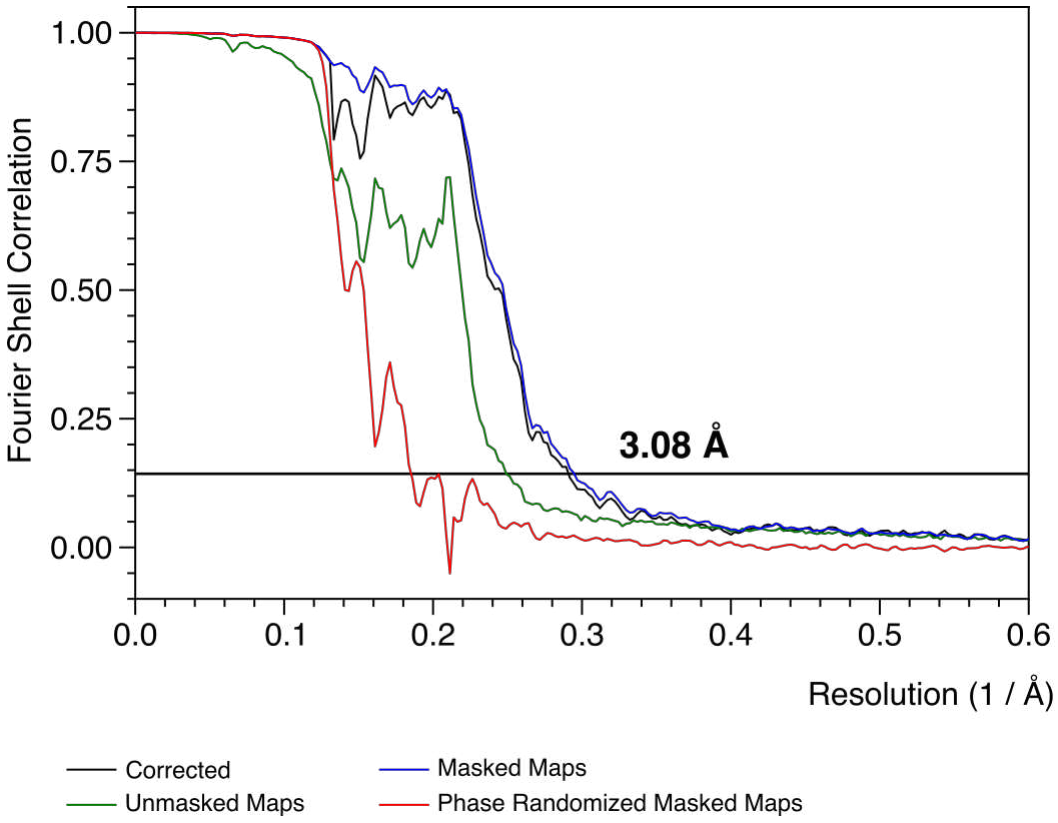
PrP Sequence Assignment	Average Masses (Da)		
	Observed	Expected	Error
73-231	17,983.80	17,983.88	-0.08
81-231	17,176.60	17,177.04	-0.44
85-231	16,756.80	16,757.60	-0.8
89-231	16,399.80	16,400.23	-0.43
91-231	16,214.50	16,215.05	-0.55
116-231	13,633.70	13,634.15	-0.45
118-231	13,491.60	13,491.99	-0.39
133-231	12,200.90	12,201.49	-0.59
134-231	12,070.00	12,070.29	-0.29
153-231	9,602.20	9,602.63	-0.43



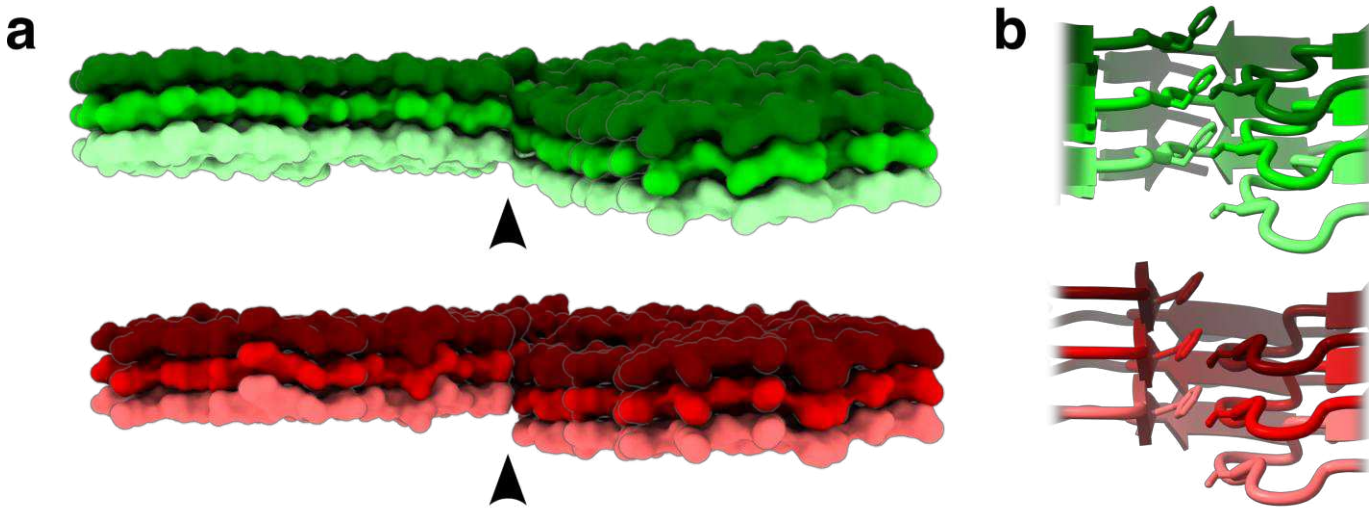
Supplementary Figure 2: **Mass spectrometry analysis of prion rods purified from sPMCA.** Purified fibrils from RML-seeded sPMCA reaction (generation 7) after seeding with RML as analysed by intact liquid chromatography-mass spectrometry. (a) Combined raw mass spectrum of principle chromatography peak with clear resolution of individual components of isotopic envelope (inset). (b) Deconvoluted mass spectrum of (a) with those peaks with normalised intensity greater than 10% of principle peak annotated (black arrows). (c) PrP sequence assignments with observed and expected average masses for peaks annotated in (b). (d) Relative abundance of PrP species assigned in (c).



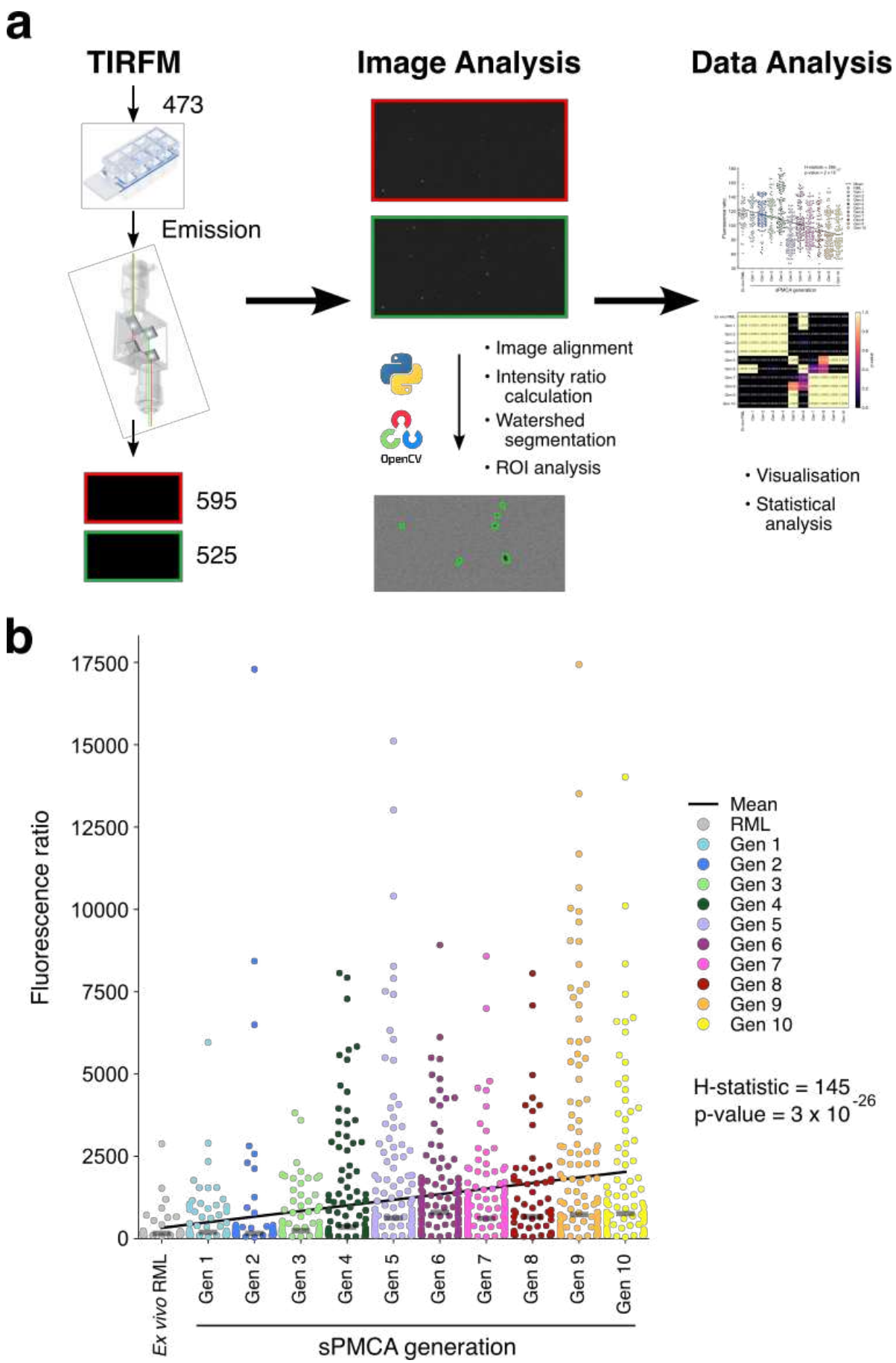
Supplementary Figure 3: Alignment of 2D-classes from sPMCA fibril cryo-EM imaging with an untwisted ex vivo RML fibril model. Cross-sectional (left) and lateral (middle) projections of an untwisted ex vivo RML fibril model rotated at 5° intervals were aligned with 2D classes obtained from cryo-EM images of sPMCA fibrils (right). Class matching was used to assign rotational angles and lateral offset values for back-projection in 3D space and subsequent refinement using RELION 5.0.



Supplementary Figure 4: Fourier Shell Correlation (FSC) plot for independent half-reconstructions, determined in Relion 5.0.



Supplementary Figure 5: (a) Side view of sPMCA derived prion fibril fold (red) and ex vivo RML (green) showing staggered fibril conformation at the inter-lobe interface (arrows). (b) Zoomed region of the inter-lobe interface showing inter-rung stagger and hydrophobic interactions of V120 and F174.



Supplementary Figure 6: (a) Workflow of single particle spectral fingerprinting using Amytracker540 dye. (b) Size distribution of prion particles in serial PMCA.

Supplementary Files

This is a list of supplementary files associated with this preprint. Click to download.

- ValidationReportsPMCARMLPDB29BREMD57062.pdf
- rs.pdf